

# Enhanced Spin Hall Ratio in Two-Dimensional Semiconductors

Jiaqi Zhou,<sup>1,\*</sup> Samuel Poncé,<sup>1,2,3,†</sup> and Jean-Christophe Charlier<sup>1,‡</sup>

<sup>1</sup>*Institute of Condensed Matter and Nanosciences (IMCN),  
Université catholique de Louvain (UCLouvain), 1348 Louvain-la-Neuve, Belgium*

<sup>2</sup>*European Theoretical Spectroscopy Facility*

<sup>3</sup>*WEL Research Institute, Avenue Pasteur 6, 1300 Wavre, Belgium*

(Dated: April 16, 2024)

The conversion efficiency from charge current to spin current via spin Hall effect is evaluated by the spin Hall ratio (SHR). Through state-of-the-art *ab initio* calculations involving both charge conductivity and spin Hall conductivity, we report the SHRs of the III-V monolayer family, revealing an ultrahigh ratio of 0.58 in the hole-doped GaAs monolayer. In order to find more promising 2D materials, a descriptor for high SHR is proposed and applied to a high-throughput database, which provides the fully-relativistic band structures and Wannier Hamiltonians of 216 exfoliable monolayer semiconductors and has been released to the community. Among potential candidates for high SHR, the MXene monolayer  $\text{Sc}_2\text{CCl}_2$  is identified with the proposed descriptor and confirmed by computation, demonstrating the descriptor validity for high SHR materials discovery.

*Introduction* – The Hall effect encompasses a wide range of phenomena which realize the conversion between various physical properties [1, 2]. The strength of Hall effect can be denoted by  $\beta = \tan(\theta_H) = E_H/E$  where  $\theta_H$  is the Hall angle,  $E_H$  is the transverse Hall field, and  $E$  is the longitudinal electric field [3]. Correspondingly, the strength of spin Hall effect (SHE) is given by the spin Hall ratio (SHR) as  $\xi = \tan(\theta_{SH}) = \frac{2e}{\hbar} \left| \frac{J_s}{J_c} \right|$  where  $\theta_{SH}$  is the spin Hall angle,  $J_s$  is the transverse spin Hall current density, and  $J_c$  is the longitudinal charge current density. SHR is often used as a proxy to indicate the charge-to-spin conversion efficiency which is crucial for low-power-consumption spintronic applications [4–6]. Indeed, when  $\theta_{SH}$  is small, the first-order Taylor polynomial gives  $\xi \approx \theta_{SH}$ , which is a good approximation for the bulk semiconductors and metals where  $\xi \sim 0.01$  [7–9]. Recently, enhanced SHR has been found in van der Waals materials with strong spin-orbit coupling (SOC). Huge SHRs over 10 are reported in topological insulators [10, 11] while large SHR  $\sim 0.5$  in  $\text{MoTe}_2$  and  $\text{WTe}_2$  Weyl semimetals have also been theoretically and experimentally identified [12–15]. However, the relative abundance of topological materials is around 1% [16, 17], limiting material options for device manufacturing. The various two-dimensional (2D) materials enable a preferable compatibility with the integrated circuit [18] with desirable properties. For instance, the  $\text{MoS}_2$  monolayer can exhibit  $\xi = 0.14$  induced by the Rashba-Edelstein effect [19]. Note that large  $\xi$  will break the approximation  $\xi \approx \theta_{SH}$  and therefore the spin Hall ratio rather than the spin Hall angle should be used to denote the ratio of spin current to charge current. 2D materials composed of heavy atoms are promising for SHE [20, 21] since the strong SOC can induce a large spin Hall conductivity (SHC), and doping is an effective way to manipulate the transport behaviors in semiconductors. Both factors can promote the SHR enhancement in 2D semiconductors.

Although charge transport and SHC have been separately investigated in 2D materials [22–26], the study of SHR remains elusive due to the multidisciplinary complexity involving the electron-phonon interaction (EPI) for electron motion [27, 28] and SOC for spin transport [4, 5]. In this Letter, we report the spin Hall ratios in monolayer semiconductors using density

functional theory (DFT) [29], density functional perturbation theory (DFPT) [30], and Wannier functions [31]. The family of III-V monolayer semiconductors (MX, M=Ga, In, and X = As, Sb) are investigated. In the hole-doped regimes, the charge conductivities are significantly suppressed by the strong inter-peak scattering, while high SHCs occur due to the strong SOC, yielding an ultrahigh SHR of  $\xi = 0.58$  in GaAs monolayer. Taking the transport behaviors of III-V monolayers as a prototype, we propose a general descriptor for the high SHR based on the electronic structures. To validate the generality of this descriptor, we create a high-throughput database by performing fully-relativistic DFT calculations and Wannierizations on 216 monolayer semiconductors, whose electronic band structures, effective masses, and SHCs have been calculated. The database is screened by the descriptor and suggests two MXene candidates,  $\text{Sc}_2\text{CCl}_2$  and  $\text{Y}_2\text{CBr}_2$  monolayers. The charge conductivities are investigated in both materials, confirming high SHR and validating the proposed SHR descriptor.

*Methods* – Charge transport properties are computed by solving the iterative Boltzmann transport equation [32] and the spin Hall conductivity using the Kubo formula [33] as implemented in the QUANTUM ESPRESSO [34], EPW [35, 36], and WANNIER90 [37] codes considering SOC and 2D Coulomb truncation [38]. The high-throughput calculations are implemented using AiiDA [39], PSEUDO DOJO [40], and the MC2D database [41, 42]. Additional details are provided in Secs. S1 and S7 of the Supplemental Material (SM) [43]. For the III-V and MXene monolayers investigated in this work, details of the relaxed atomic structures, effective masses, densities of states (DOS), doping levels, and electron and phonon dispersions are given in SM [43]. The input and output files, pseudopotentials, as well as Wannier Hamiltonians and band structures of 216 monolayer semiconductors, are provided on Materials Cloud Archive [44].

*Charge transport* – The phonon-limited charge conductivity in doped 2D semiconductor is calculated as [32]

$$\sigma_{\alpha\beta} = \frac{-e}{\text{SUC}} \sum_n \int \frac{d^2\mathbf{k}}{\Omega\text{BZ}} v_{n\mathbf{k}\alpha} \partial_{E_\beta} f_{n\mathbf{k}}, \quad (1)$$

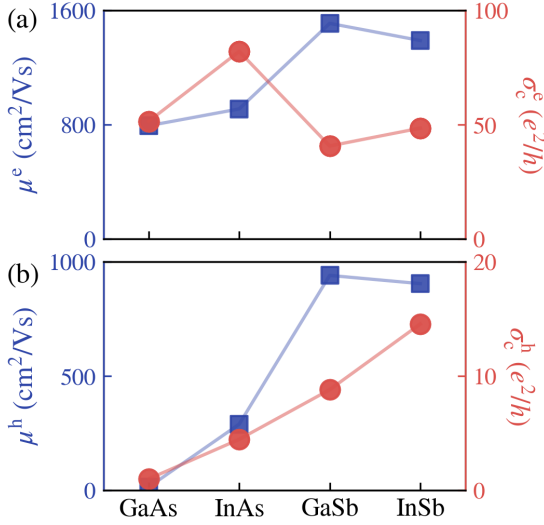


FIG. 1. Drift mobilities of pristine semiconductors (blue) and charge conductivities of doped systems (red) at 300 K.  $\mu^e$  and  $\mu^h$  denote (a) electron and (b) hole mobilities of pristine semiconductors with square markers (left axis),  $\sigma_c^e$  and  $\sigma_c^h$  indicate the charge conductivities of (a) electron-doped and (b) hole-doped systems with circle markers (right axis).

where  $\alpha$  and  $\beta$  are Cartesian directions,  $S^{\text{uc}}$  is the unit cell area,  $\Omega^{\text{BZ}}$  is the first Brillouin zone area, and  $v_{n\mathbf{k}\alpha} = \hbar^{-1} \partial \varepsilon_{n\mathbf{k}} / \partial k_\alpha$  is the band velocity,  $n$  is the band index. The linear variation of the electronic occupation function  $f_{n\mathbf{k}}$  in response to  $\mathbf{E}$ ,  $\partial E_\beta f_{n\mathbf{k}}$ , can be obtained by solving the Boltzmann transport equation [Eq. (S1) of SM [43]] which induces the scattering rate given by

$$\tau_{n\mathbf{k}}^{-1} = \frac{2\pi}{\hbar} \sum_{m\nu} \int \frac{d^2\mathbf{q}}{\Omega^{\text{BZ}}} |g_{m\nu\nu}(\mathbf{k}, \mathbf{q})|^2 \times [(n_{\mathbf{q}\nu} + 1 - f_{m\mathbf{k}+\mathbf{q}}^0) \delta(\varepsilon_{n\mathbf{k}} - \varepsilon_{m\mathbf{k}+\mathbf{q}} - \hbar\omega_{\mathbf{q}\nu}) + (n_{\mathbf{q}\nu} + f_{m\mathbf{k}+\mathbf{q}}^0) \delta(\varepsilon_{n\mathbf{k}} - \varepsilon_{m\mathbf{k}+\mathbf{q}} + \hbar\omega_{\mathbf{q}\nu})], \quad (2)$$

where  $g_{m\nu\nu}(\mathbf{k}, \mathbf{q})$  is the electron-phonon matrix element with phonon frequency  $\omega_{\mathbf{q}\nu}$ ,  $\varepsilon_{n\mathbf{k}}$  and  $\varepsilon_{m\mathbf{k}+\mathbf{q}}$  are eigenvalues,  $f_{n\mathbf{k}}$  is the Fermi-Dirac distribution,  $n_{\mathbf{q}\nu}$  is the Bose-Einstein distribution. The drift mobility of pristine semiconductor is related to the charge conductivity as  $\mu_{\alpha\beta} = \sigma_{\alpha\beta} / (en^c)$  when the carrier density  $n^c$  is very small such that ionized impurity scattering can be neglected. Due to crystal symmetry,  $\mu = \mu_{xx} = \mu_{yy}$ ,  $\sigma = \sigma_{xx} = \sigma_{yy}$  in all the III-V monolayers. Note that  $\mu$  and  $\sigma$  are separately calculated since in this work, heavy dopings are applied, thus breaking the linear relation between them [45]. In the following,  $\sigma_c$  is used to denote the charge conductivity.

Figure 1 presents the room-temperature mobilities of the pristine monolayers and the conductivities of doped systems. All the materials exhibit high electron mobilities, thanks to the small electron effective mass and the single valley in the conduction bands. More variations in the hole mobility are observed due to the multi-peak band structures. The two ar-

senides present different mobilities of 14 and 289, while two similar values, 940 and 904, are observed in the antimonides. A detailed analysis of mobility mechanisms is given in our accompanying manuscript [46]. In this paper, the conductivities in doped III-V monolayers are extensively explained.

Doping is a practical method to tune the transport properties of semiconductors [47]. Sufficient carriers are induced by heavy doping which turns semiconductors into metallic systems where SHE can occur. Considering the DOS, an electron doping of  $1 \times 10^{13} \text{ cm}^{-2}$  and a hole doping of  $2 \times 10^{13} \text{ cm}^{-2}$  are respectively applied to the III-V monolayers, whose structures have been relaxed again. The main impact of such doping is the shift of Fermi energy ( $E_F$ ) by a few hundred meV, leaving the crystal structure and electronic bands nearly unaffected as verified by Section S2 of SM [43], where the phonon dispersions are also presented. The absence of imaginary frequency in phonon dispersions demonstrates the stabilities of doped systems. Interestingly, an electron-hole asymmetry occurs in the phonon dispersions of all the III-V monolayers: the phonon dispersion is weakly affected by electron doping, while softening specifically occurs in the hole doping case. The asymmetry can be explained by the difference in conduction and valence bands. For the electron doping, the  $\Gamma$  valley is occupied, leading to a moderate screening of the EPI by free carriers and a decrease of the EPI. In contrast, multiple inequivalent peaks are occupied at room temperature in the case of hole doping. In this regime, the EPI is *strengthened* with doping due to the charge transfer between inequivalent peaks with opposite deformation potentials [48–50], resulting in the observed phonon softening in the optical modes. In a nutshell, the asymmetry in the conduction and valence bands leads to the reduced EPI in electron-doped systems as verified by the high  $\sigma_c^e$  in Fig. 1(a) and the enhanced EPI in hole-doped systems as verified by the low  $\sigma_c^h$  in Fig. 1(b).

It is expected that the charge conductivity should be proportional to the carrier mobility. However, Fig. 1(a) illustrates that GaAs presents a much lower  $\mu^e$  but higher  $\sigma_c^e$  than GaSb with the same electron doping. In Fig. 1(b), GaSb shows a high  $\mu^h$  but a low  $\sigma_c^h$  with the hole doping. These unusual behaviors will be interpreted within the self-energy relaxation time approximation [32], where the conductivity is inversely proportional to the scattering rate and directly proportional to carrier velocity. Considering the Fermi-Dirac distribution at equilibrium and 300 K, we define the  $\mathbf{k}$ -resolved scattering rates as  $\tau_{\mathbf{k}}^{-1} = \sum_n \frac{\partial f_0}{\partial \varepsilon_{n\mathbf{k}}} \tau_{n\mathbf{k}}^{-1}$ , and  $\mathbf{k}$ -resolved velocities as  $v_{\mathbf{k}} = \sum_n v_{n\mathbf{k}}$ , where  $n$  denotes the number of bands involved in the transport. Figure 2 compares the electronic structures,  $\tau_{\mathbf{k}}^{-1}$ , and  $v_{\mathbf{k}}$  of doped GaAs and GaSb. Before doping, both pristine GaAs and GaSb exhibit a Rashba splitting [51] in the conduction band minimum (CBM) which can be regarded as a single valley. After electron doping, Fig. 2(a) shows that for GaAs, the single valley is preserved in the Fermi surface window [ $E_F - 0.3 \text{ eV}$ ,  $E_F + 0.3 \text{ eV}$ ], while Fig. 2(d) shows that for GaSb, more states around M and K points enter into the window, leading to enhanced scatterings with states that possess low velocities. As a result,  $\sigma_c^e$  in GaSb is reduced as shown in Fig. 1(a). The surprising behaviors of  $\mu^h$  and  $\sigma_c^h$  of

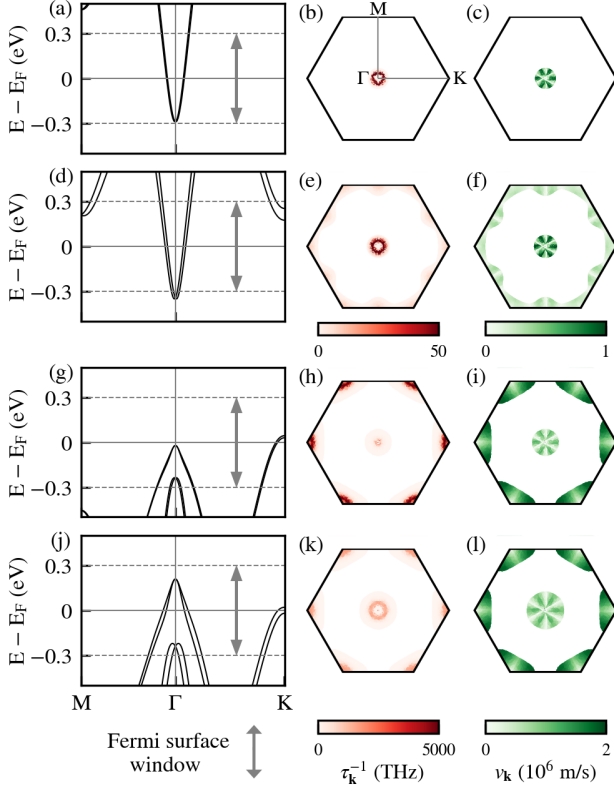


FIG. 2. Electronic structures,  $k$ -resolved scattering rates, and  $k$ -resolved velocities for charge conductivities of (a)-(c) electron-doped GaAs, (d)-(f) electron-doped GaSb, (g)-(i) hole-doped GaAs, and (j)-(l) hole-doped GaSb. The vertical arrow denotes the Fermi surface window, where 0.3 eV has been validated for the transport property convergence.

GaSb in Fig. 1(b) can be attributed to the doping-induced  $E_F$  shift. The valence band maximum (VBM) of pristine GaAs locates at K points, leading to a multi-peak band structure and a high DOS around VBM, thus the hole doping can only induce a small  $E_F$  shift as shown in Fig. 2(g). Besides, the spin-orbit splitting at K in the electronic band is 12 meV, which matches well with the phonon energy at K in the phonon dispersion. Considering momentum and energy conservations, the strong inter-peak scatterings between the K and K' peaks are allowed in both pristine and hole-doped GaAs. Differently, the VBM in pristine GaSb is located at  $\Gamma$ , which is a single peak for the hole mobility and leads to a high  $\mu^h$ . The single-peak band structure gives a small DOS around VBM, thus a large  $E_F$  shift of 0.21 eV is induced by the hole doping as shown in Fig. 2(j), leading the states around K to dominate the scattering. Considering the low velocities at K points,  $\sigma_c^h$  is greatly reduced compared with  $\mu^h$  in GaSb. It should be noted that for GaSb, the spin-orbit splitting at K is 40 meV, mismatching the phonon energy, thus the inter-peak scattering between K and K' is weakened compared with GaAs, as shown by the colors in Figs. 2(h) and (k). The discussions above demonstrate that doping is an effective way to manipulate the electronic structure, further controlling the EPI and charge conductivity in semiconductors.

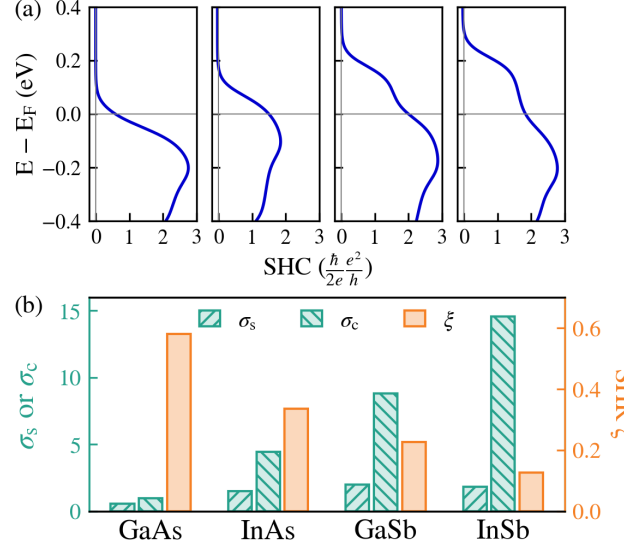


FIG. 3. (a) Energy-dependent SHCs at 300 K. (b) SHCs  $\sigma_s$  at  $E_F$  (unit:  $(\hbar/2e)e^2/h$ ), charge conductivities  $\sigma_c$  (unit:  $e^2/h$ ), and SHRs  $\xi$  of hole-doped GaAs, InAs, GaSb, and InSb, respectively.

*Spin Hall conductivity* – SHE is composed of intrinsic and extrinsic contributions. The former is defined by the Kubo formula, and the latter is due to the skew-scattering and side-jump mechanisms, strongly dependent on disorder [52–54]. In this work, we focus on the intrinsic SHC in a weak scattering limit. With spin current along  $x$ , electric field along  $y$ , and spin orientation along  $z$  direction, the intrinsic SHC is calculated using Kubo formula [33]:

$$\sigma_s = \frac{\hbar}{2e} \frac{e^2}{\hbar} \int_{\text{BZ}} \frac{d^2\mathbf{k}}{(2\pi)^2} \Omega_s(\mathbf{k}), \quad (3)$$

where  $\Omega_s(\mathbf{k}) = \sum_n f_{n\mathbf{k}} \Omega_{s,n}(\mathbf{k})$  is the spin Berry curvature (SBC) with  $f_{n\mathbf{k}}$  at 300 K and the band-resolved SBC as

$$\Omega_{s,n}(\mathbf{k}) = \hbar^2 \sum_{m \neq n} \frac{-2 \text{Im}[\langle n\mathbf{k} | \hat{j}_z | m\mathbf{k} \rangle \langle m\mathbf{k} | \hat{v}_y | n\mathbf{k} \rangle]}{(\varepsilon_{n\mathbf{k}} - \varepsilon_{m\mathbf{k}})^2 + \eta^2}, \quad (4)$$

where  $\hat{j}_z = \frac{1}{2} \{ \hat{\sigma}_z \hat{v}_x + \hat{v}_x \hat{\sigma}_z \}$  is the spin current operator,  $\hat{\sigma}_z$  is the Pauli operator,  $\hat{v}_x$  and  $\hat{v}_y$  are velocity operators. Considering the SOC strength in all the materials, a broadening of  $\eta = 2$  meV is used as a weak scattering in spin transport [55]. Due to the low conductivities, the hole-doped systems are more promising for high SHRs, thus III-V monolayer with  $2 \times 10^{13} \text{ cm}^{-2}$  hole doping are targeted for SHCs, and this doping level has been realized in 2D systems [48, 56]. Figure 3(a) presents the energy-dependent SHCs of hole-doped materials at room temperature. GaAs exhibits  $\sigma_s^h = 0.6 (\hbar/2e)e^2/h$  due to the small  $E_F$  shift induced by doping. More prominently, SHCs of InAs, GaSb, and InSb can reach up to 1.5, 2.0, and 1.8  $(\hbar/2e)e^2/h$ , respectively. For comparison, MoS<sub>2</sub> monolayer only reaches  $\sigma_s^h \approx 0.2 (\hbar/2e)e^2/h$  [22]. The high SHCs in hole-doped III-V monolayers are attributed to the in-gap  $E_F$  location, as shown in

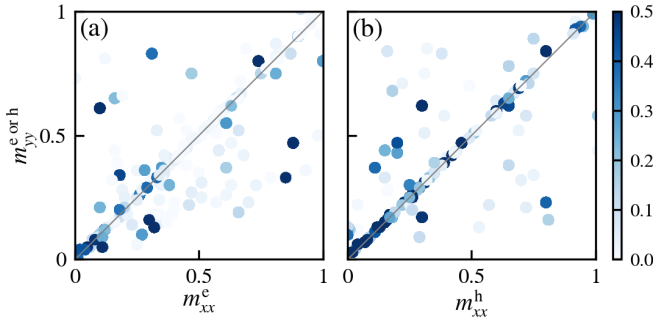


FIG. 4. Electron (a) and hole (b) effective masses of 216 monolayer semiconductors in unit of  $m_0$ , SHC values are given by the color bar in units of  $(\hbar/2e)e^2/h$  in electron- and hole-doped systems, respectively. Diagonal lines denote isotropic materials where  $m_{xx} = m_{yy}$ . The doping concentration is  $2 \times 10^{13} \text{ cm}^{-2}$  for both carriers.

Fig. 2(j). The spin-orbit gap separates the positive and negative SBC. When the  $E_F$  locates inside the spin-orbit gap, SHC, as the integration over the Fermi sea of SBC, can be maximized by the sign-invariant SBC over all the  $k$ -points. The SBC decompositions of all the materials are presented in Section S5 of SM [43]. For GaAs, the SBC originates from both K and  $\Gamma$  points, while for the others, the SBC mainly stems from the  $\Gamma$  point due to the in-gap  $E_F$  at  $\Gamma$ . The discussions above highlight that the doping in semiconductors can yield large SHCs in III-V monolayers.

*Spin Hall ratio* – With the charge conductivities  $\sigma_c$  and spin Hall conductivities  $\sigma_s$ , the spin Hall ratio  $\xi = \frac{2e}{\hbar} \left| \frac{\sigma_s}{\sigma_c} \right|$  can be discussed in hole-doped systems. Figure 3(b) shows that large  $\sigma_s^h$  values are found in antimonides which also possess fairly large  $\sigma_c^h$ , as a result, GaSb and InSb exhibit  $\xi^h = 0.23$  and 0.13, respectively. More importantly, hole-doped arsenides are perfect candidates with high SHCs and low charge transports, yielding exceptional  $\xi^h = 0.58$  and 0.34 in GaAs and InAs, respectively. Compared with heavy metals where  $\xi \approx 0.01$ , the hole-doped GaAs and other III-V monolayers exhibit great potential for efficient charge-to-spin conversion.

*Spin Hall ratio descriptor* – Taking the transport behaviors in III-V monolayers as a prototype, a descriptor to enhance SHR can be proposed. The idea is to decrease the charge conductivity as well as increasing SHC. Large effective mass reduces  $\sigma_c$  via lowering down the carrier velocity. As discussed in Fig. 2, the band structure with multiple extrema around  $E_F$  can enhance scattering, and the matching between energy difference  $\Delta\varepsilon_{nK}$  and phonon energy  $\omega_{nK}$  is a plus to strengthen the inter-peak scattering, note that K can be any  $k$ -point away from  $\Gamma$  in the BZ. Regarding the SHC, the energy-dependent SHCs have shown the importance of the  $E_F$  location. Overall, a descriptor for high SHR can be proposed: large effective mass, multiple inequivalent extrema in the electronic band structure, and a  $E_F$  located inside the spin-orbit gap. It should be stressed that within a limited doping concentration, there is a competition between the first two conditions and the last one, since flat and multiple band extrema would induce a large DOS, which

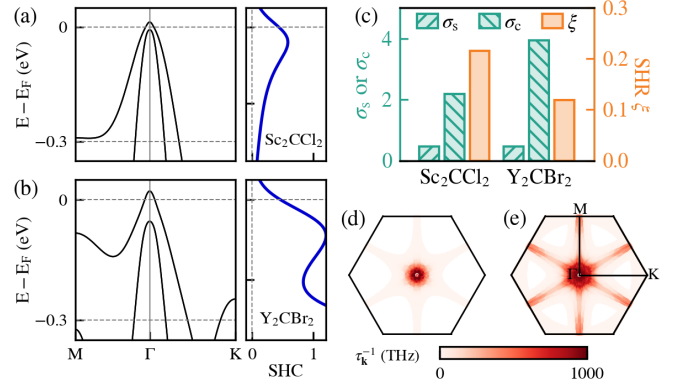


FIG. 5. Hole-doped  $\text{Sc}_2\text{CCl}_2$  and  $\text{Y}_2\text{CBr}_2$  monolayers: (a)-(b) Electronic structures and energy-dependent SHCs in units of  $(\hbar/2e)e^2/h$ . (c) Spin Hall and charge conductivities as well as SHRs. (d)-(e) Scattering rates  $\tau_{\mathbf{k}}^{-1}$ .

hinders the tuning of  $E_F$ . Consequently, a delicate balance between  $\sigma_c$  and  $\sigma_s$  is essential.

*High-throughput calculations* – Potential candidates for high SHR can be found by screening a database with the aforementioned descriptor. Focusing on the 2D materials, we perform fully-relativistic high-throughput calculations for exfoliable monolayers. From the MC2D database [41, 42], all the rare-earth free materials with up to 6 atoms per unit cell are considered, yielding 216 semiconductors which are employed for the fully-relativistic DFT calculations and Wannierizations. Figure 4 shows the electron and hole effective masses of all the semiconductors, as well as SHC values in the doped systems. The effective mass is calculated by  $m_{\alpha\alpha} = (\frac{1}{\hbar^2} \frac{d^2\varepsilon}{dk_\alpha^2})^{-1}$  ( $\alpha = x, y$ ) through the interpolation around CBM and VBM respectively for electron and hole. Overall, the hole presents larger effective mass than the electron, and hole-doped materials exhibit larger SHC values. Nevertheless, many materials with high SHCs present small effective masses, populated at the left lower corner in Fig. 4(b). Still, by setting the screening conditions as  $m_{xx} \approx m_{yy} > 0.5 m_0$ , multiple band extrema around  $E_F$ , and  $\text{SHC} > 0.4 (\hbar/2e)e^2/h$ , two MXene monolayers are selected as candidates,  $\text{Sc}_2\text{CCl}_2$  and  $\text{Y}_2\text{CBr}_2$ . Quality assessment of Wannier Hamiltonians, effective masses, doped SHCs, energy gaps, and band structures of all the 216 semiconductors are reported in Section S7 of SM [43]. Notably, 97% materials present the interpolation error of less than 10 meV for bands below CBM + 1 eV, demonstrating the high accuracy of the database.

$\text{Sc}_2\text{CCl}_2$  and  $\text{Y}_2\text{CBr}_2$  present similarities since they are composed by elements from the same group. Both are easily exfoliable with a small interlayer binding energy [42]. After a full relaxation including the hole doping, both present a P-3m1 space group, and their mechanical stabilities have been validated by phonon dispersion without imaginary frequency as given in Fig. S10 of SM [43]. Figures 5(a)-(b) illustrate the hole-doped band structures of  $\text{Sc}_2\text{CCl}_2$  and  $\text{Y}_2\text{CBr}_2$ .  $m_{xx} = m_{yy} \approx 0.7 m_0$  on the top band. Heavy elements lead to the SOC splitting

and two peaks around the  $\Gamma$  point.  $E_F$  locates inside the gap, leading to  $\sigma_s^h = 0.5 (\hbar/2e)e^2/h$ . Interestingly, the band structures can be modeled by the Luttinger Hamiltonian, which shows robust SHC against disorder [57]. Benefiting from all the advantages above, the SHR in  $\text{Sc}_2\text{CCl}_2$  is computed to be  $\xi^h = 0.22$ , and  $\xi^h = 0.12$  for  $\text{Y}_2\text{CBr}_2$  as shown in Fig. 5(c). The discrepancy in SHR values is attributed to the different charge transports. Figures 5(d)-(e) show that the scattering in  $\text{Sc}_2\text{CCl}_2$  reaches up to 836 THz thanks to its small SOC gap of 20 meV matching phonon energy, while the scattering in  $\text{Y}_2\text{CBr}_2$  is limited to 370 THz due to its large gap of 75 meV. As a result,  $\text{Sc}_2\text{CCl}_2$  presents lower  $\sigma_c^h$  and higher SHR. The discussions above validate the SHR descriptor and reveal  $\text{Sc}_2\text{CCl}_2$  as a potential candidate for high SHR. By expanding the high-throughput calculations database, materials with more ideal electronic structures could be found to further enhance SHR.

*Experimental feasibility* – Charge-to-spin conversion has been realized in  $\text{MoS}_2$  and  $\text{WSe}_2$  monolayers grown by chemical vapor deposition [19]. Since the first synthesis of 2D AlN layers by metal organic deposition [58], many efforts have been devoted to the synthesis of other 2D III-V materials [59, 60]. For example, GaSb films can be grown via a seeded lateral epitaxy, and the free-standing crystalline GaSb can be exfoliated from these films [61]. Moreover, 2D InAs flakes with high crystalline quality have been synthesized through van der Waals epitaxy with a thickness down to 4.8 nm [62]. Due to chemical similarity in one family, we expect similar techniques can be applied to the other III-V monolayers. Two promising materials  $\text{Sc}_2\text{CCl}_2$  and  $\text{Y}_2\text{CBr}_2$  are easily exfoliable from their van der Waals bulk compounds [42]. Finally, the doping levels proposed in this work can be realized via the advanced technique of electron beam, which implements the doping of  $1.7 \times 10^{13} \text{ cm}^{-2}$  in 2D systems [56]. The doped state persists even after removing the electron beam and back-gate voltage, and the process is reversible and repeatable [56]. Moreover, the doping level over  $5 \times 10^{13} \text{ cm}^{-2}$  has been realized in  $\text{MoS}_2$  monolayers via the ionic-liquid gate [48].

In conclusion, 2D materials with high spin Hall ratios have been found using a multidisciplinary investigation involving charge transport, spin Hall conductivity, and high-throughput database. The hole-doped GaAs monolayer presents an ultra-high SHR of  $\xi = 0.58$ , attributed to the strong scattering and the high SHC. A SHR descriptor is proposed and validated by a high-throughput database of 216 exfoliable monolayer semiconductors, suggesting a new promising material  $\text{Sc}_2\text{CCl}_2$ . Besides, this database is fully released to the community. This work reveals potential 2D materials for efficient charge-to-spin conversion, providing a guideline for materials discovery in spintronics.

The authors would like to thank Xi Dai, Matteo Giantomassi, and Junfeng Qiao for fruitful discussions. S. P. acknowledges the support from the Fonds de la Recherche Scientifique de Belgique (F.R.S.-FNRS). J. Z. and J.-C.C. acknowledge financial support from the Fédération Wallonie-Bruxelles through the ARC Grant “DREAMS” (No. 21/26-116), from the EOS project “CONNECT” (No. 40007563), and from the Belgium F.R.S.-FNRS through the research project (No. T.029.22F).

Computational resources have been provided by the PRACE award granting access to MareNostrum4 at Barcelona Supercomputing Center (BSC), Spain and Discoverer in SofiaTech, Bulgaria (OptoSpin project ID. 2020225411), and by the Consortium des Équipements de Calcul Intensif (CÉCI), funded by the F.R.S.-FNRS under Grant No. 2.5020.11 and by the Walloon Region, as well as computational resources awarded on the Belgian share of the EuroHPC LUMI supercomputer.

\* [jiaqi.zhou@uclouvain.be](mailto:jiaqi.zhou@uclouvain.be)

† [samuel.ponce@uclouvain.be](mailto:samuel.ponce@uclouvain.be)

‡ [jean-christophe.charlier@uclouvain.be](mailto:jean-christophe.charlier@uclouvain.be)

- [1] J. Inoue and H. Ohno, *Science* **309**, 2004 (2005).
- [2] C.-Z. Chang and M. Li, *J. Phys.: Condens. Matter* **28**, 123002 (2016).
- [3] N. W. Ashcroft and N. D. Mermin, *Solid State Physics* (Harcourt College publisher, 1976).
- [4] J. Sinova, S. O. Valenzuela, J. Wunderlich, *et al.*, *Rev. Mod. Phys.* **87**, 1213 (2015).
- [5] A. Manchon, J. Železný, I. M. Miron, *et al.*, *Rev. Mod. Phys.* **91**, 035004 (2019).
- [6] Z. Guo, J. Yin, Y. Bai, *et al.*, *Proc. IEEE* **109**, 1398 (2021).
- [7] I. Žutić, J. Fabian, and S. Das Sarma, *Rev. Mod. Phys.* **76**, 323 (2004).
- [8] K. Olejník, J. Wunderlich, A. C. Irvine, *et al.*, *Phys. Rev. Lett.* **109**, 076601 (2012).
- [9] X. Tao, Q. Liu, B. Miao, *et al.*, *Sci. Adv.* **4**, eaat1670 (2018).
- [10] M. De, R. Grassi, J.-Y. Chen, *et al.*, *Nat. Mater.* **17**, 800 (2018).
- [11] N. H. D. Khang, Y. Ueda, and P. N. Hai, *Nat. Mater.* **17**, 808 (2018).
- [12] J. Zhou, J. Qiao, A. Bournel, and W. Zhao, *Phys. Rev. B* **99**, 060408(R) (2019).
- [13] B. Zhao, D. Khokhriakov, Y. Zhang, *et al.*, *Phys. Rev. Res.* **2**, 013286 (2020).
- [14] M. Vila, C.-H. Hsu, J. H. Garcia, *et al.*, *Phys. Rev. Res.* **3**, 043230 (2021).
- [15] P. Song, C.-H. Hsu, G. Vignale, *et al.*, *Nat. Mater.* **19**, 292 (2020).
- [16] A. Marrazzo, M. Gibertini, D. Campi, *et al.*, *Nano Lett.* **19**, 8431 (2019).
- [17] D. Grassano, N. Marzari, and D. Campi, *Phys. Rev. Mater.* **8**, 024201 (2024).
- [18] C. Dorow, K. O’Brien, C. H. Naylor, *et al.*, *IEEE Transactions on Electron Devices* **68**, 6592 (2021).
- [19] Q. Shao, G. Yu, Y.-W. Lan, *et al.*, *Nano Lett.* **16**, 7514 (2016).
- [20] H. Wang, H. Lu, Z. Guo, *et al.*, *Nat. Commun.* **14**, 1 (2023).
- [21] H. Wang, H. Wu, J. Zhang, *et al.*, *Nat. Commun.* **14**, 1 (2023).
- [22] W. Feng, Y. Yao, W. Zhu, *et al.*, *Phys. Rev. B* **86**, 165108 (2012).
- [23] T. Sohier, D. Campi, N. Marzari, and M. Gibertini, *Phys. Rev. Mater.* **2**, 114010 (2018).
- [24] H. Wang, P. Gopal, S. Picozzi, *et al.*, *npj Comput. Mater.* **6**, 1 (2020).
- [25] J. Backman, Y. Lee, and M. Luisier, *Solid-State Electron.* **198**, 108461 (2022).
- [26] C. Zhang, R. Wang, H. Mishra, and Y. Liu, *Phys. Rev. Lett.* **130**, 087001 (2023).
- [27] A. Cepellotti, J. Coulter, A. Johansson, *et al.*, *J. Phys.: Mater.* **5**, 035003 (2022).
- [28] F. Giustino, *Rev. Mod. Phys.* **89**, 015003 (2017).
- [29] W. Kohn, *Rev. Mod. Phys.* **71**, 1253 (1999).
- [30] S. Baroni, S. de Gironcoli, A. Dal Corso, and P. Giannozzi, *Rev.*

- Mod. Phys.* **73**, 515 (2001).
- [31] N. Marzari, A. A. Mostofi, J. R. Yates, *et al.*, *Rev. Mod. Phys.* **84**, 1419 (2012).
- [32] S. Ponc e, W. Li, S. Reichardt, and F. Giustino, *Rep. Prog. Phys.* **83**, 036501 (2020).
- [33] J. Qiao, J. Zhou, Z. Yuan, and W. Zhao, *Phys. Rev. B* **98**, 214402 (2018).
- [34] P. Giannozzi, O. Andreussi, T. Brumme, *et al.*, *J. Phys.: Condens. Matter* **29**, 465901 (2017).
- [35] S. Ponc e, E. R. Margine, C. Verdi, and F. Giustino, *Comput. Phys. Commun.* **209**, 116 (2016).
- [36] H. Lee, S. Ponc e, K. Bushick, *et al.*, *npj Comput. Mater.* **9**, 1 (2023).
- [37] G. Pizzi, V. Vitale, R. Arita, *et al.*, *J. Phys.: Condens. Matter* **32**, 165902 (2020).
- [38] T. Sohler, M. Calandra, and F. Mauri, *Phys. Rev. B* **96**, 075448 (2017).
- [39] S. P. Huber, S. Zoupanos, M. Uhrin, *et al.*, *Sci. Data* **7**, 1 (2020).
- [40] M. J. van Setten, M. Giantomassi, E. Bousquet, *et al.*, *Comput. Phys. Commun.* **226**, 39 (2018).
- [41] N. Mounet, M. Gibertini, P. Schwaller, *et al.*, *Nat. Nanotechnol.* **13**, 246 (2018).
- [42] D. Campi, N. Mounet, M. Gibertini, *et al.*, *ACS Nano* **17**, 11268 (2023).
- [43] J. Zhou, S. Ponc e, and J.-C. Charlier, Supplemental Material (2024).
- [44] J. Zhou, S. Ponc e, and J.-C. Charlier, *Materials Cloud Archive*.
- [45] N. Ma and D. Jena, *Phys. Rev. X* **4**, 011043 (2014).
- [46] J. Zhou, S. Ponc e, and J.-C. Charlier, Guidelines for accurate and efficient calculations of mobilities in two-dimensional materials (accompanying manuscript) (2024).
- [47] S. S. Awate, B. Mostek, S. Kumari, *et al.*, *ACS Appl. Mater. Interfaces* **15**, 15785 (2023).
- [48] T. Sohler, E. Ponomarev, M. Gibertini, *et al.*, *Phys. Rev. X* **9**, 031019 (2019).
- [49] T. Sohler, P. M. M. C. de Melo, Z. Zanolli, and M. J. Verstraete, *2D Mater.* **10**, 025006 (2023).
- [50] X.-F. Liu, Z.-J. Luo, X. Zhou, *et al.*, *Chinese Physics B* **28**, 86105 (2019).
- [51] K. Wu, J. Chen, H. Ma, *et al.*, *Nano Lett.* **21**, 740 (2021).
- [52] S. Lowitzer, M. Gradhand, D. K odderitzsch, *et al.*, *Phys. Rev. Lett.* **106**, 056601 (2011).
- [53] C. Gorini, U. Eckern, and R. Raimondi, *Phys. Rev. Lett.* **115**, 076602 (2015).
- [54] U. Shashank, Y. Nakamura, Y. Kusaba, *et al.*, *Phys. Rev. B* **107**, 064402 (2023).
- [55] H. Li, H. Gao, L. P. Z arbo, *et al.*, *Phys. Rev. B* **91**, 134402 (2015).
- [56] W. Shi, S. Kahn, N. Leconte, *et al.*, *Phys. Rev. Lett.* **130**, 186204 (2023).
- [57] S. Murakami, *Phys. Rev. B* **69**, 241202 (2004).
- [58] W. Wang, Y. Zheng, X. Li, *et al.*, *Adv. Mater.* **31**, 1803448 (2019).
- [59] F. Lu, H. Wang, M. Zeng, and L. Fu, *iScience* **25**, 103835 (2022).
- [60] A. Nikolaevich Klochkov, A. Nikolaevich Vinichenko, A. Alekseevich Samolyga, *et al.*, *Appl. Surf. Sci.* **619**, 156722 (2023).
- [61] S. Manzo, P. J. Strohbeen, Z. H. Lim, *et al.*, *Nat. Commun.* **13**, 1 (2022).
- [62] J. Dai, T. Yang, Z. Jin, *et al.*, *Nano Res.* **15**, 9954 (2022).